Corrosion behavior of ferrite and aluminate refractories in cryolite-aluminium melts

R. Z. Mukhlis[1], *M. A. Rhamdhani*[2]

1. Lecturer, Fluid and Process Dynamics Research Group, Swinburne University of Technology, Hawthorn VIC 3122. Email:rmukhlis@swin.edu.au
2. Professor, Fluid and Process Dynamics Research Group, Swinburne University of Technology, Hawthorn VIC 3122. Email:arhamdhani@swin.edu.au

Keywords: Hall-Heroult, Ledge-free sidewall, Electrolysis cell.

ABSTRACT

Removing the ledge formation in the Hall-Heroult cell during the electrolysis process may significantly reduce the energy requirement of the aluminium production process. In the absence of the ledge, however, the sidewall-material types become heavily restricted since the cryolite is very corrosive at the electrolysis temperatures. This paper study the corrosion behaviour of sintered nickel ferrite, nickel aluminate, and magnesium aluminate refractories (as possible candidates for sidewall material) in molten aluminium and cryolite melts with various alumina content at 980°C. Immersion tests of refractories with various porosity were conducted to assess the suitability of the refractories in the corrosive environment of the electrolysis cells. Microstructural change of the refractory after immersion were analysed using secondary scanning electron microscopy (SEM). Sampling of the melts were taken at 0, 10 min, 30 min, and each hour up to 6h, and subsequently analysed by Inductively Coupled Plasma (ICP) spectroscopy. Based on the projected concentration of the refractories constituents in the melts, it was predicted that the corrosion rate of $NiFe_2O_4$, $NiAl_2O_4$ and $MgAl_2O_4$ in cryolite with 11wt% Al_2O_3 were 461 x 10^3, 1.03 x 10^3, and 798 x 10^3 cm/year, respectively. Much lower corrosion rate of 2.3 cm/year for $NiFe_2O_4$, 2.6 cm/year for $NiAl_2O_4$ and 0.3 cm/year for $MgAl_2O_4$ were predicted if the refractories in contact with aluminium melts. Erosion played an important role in the corrosion as the concentration of the refractory constituents in the melts were beyond its solubility limit. It is therefore crucial to increase the densities of the refractory and improve its wetting characteristics.

INTRODUCTION

Aluminium is produced commercially from alumina through the Hall-Heroult process at around 965°C where the overall chemical reaction produces metallic aluminium and carbon dioxide, as follows:

$$2Al_2O_{3(s)} + 3C_{(s)} = 4Al_{(l)} + 3CO_{2(g)} \quad (1)$$

There are two major issues suffered by the process: high cost and great environmental impact. The high cost is the consequence of its high capital cost and its eminent energy requirement. The total specific energy requirement, W_{el} (kWh/kg), of the Hall-Heroult process can be determined through the following relationship by estimating the cell voltage (Thonstad et al., 2001):

$$W_{el} = \frac{UF|V_e|}{3600 M_{Al} x_{Al} v_{Al}} = 2.98 \frac{U}{M_{Al}} \quad (2)$$

where U is the cell voltage, F is Faraday constant, $M_{(Al)}$ is the molar weight of Al, $x_{(Al)}$ is the corresponding current efficiency fraction, while $|V_e|$ and $v_{(Al)}$ are the stoichiometric numbers of electrons and of product of cathodic reaction, respectively.

By considering reaction (1) and equation (2), the theoretical energy required to produce 1 kg aluminium at 1000 °C and 100% current efficiency is 5.06 kWh. In practice, the energy consumed to produce 1 kg aluminium is ranging from 12 to 15 kWh (Schwarz, 2008; Kvande and Haupin, 2001; Haraldsson and Johansson, 2020). This energy includes the thermodynamic energy needed by the reaction, and additional energy that is required to heat the reactant from room temperature to the operational temperature and to maintain at that temperature. The necessity to have high heat loss

through the side of the cell container to form protective frozen ledge is also significantly contributing to the high energy consumption.

The significant environmental impact of the Hall-Heroult process has a strong correlation with its high energy demand, particularly if the source of electricity is coming from fossil fuel. Moreover, the fact that the Hall-Heroult process uses consumable carbon anode and the main reaction of the process produce carbon dioxide gas, induce its effect on global warming even more escalated.

It has been considered since long that the breakthrough technology of inert anode, the anode that theoretically will not be consumed during electrolysis, may revolutionise the Hall-Heroult process (Kvande and Drabloss, 2014). Not only can it alter the aluminium electrolytic process from carbon dioxide generating reaction to oxygen producing reaction (reaction 3); the implementation of inert anode will eliminate all cost associated with the consumable carbon anode. The capital cost itself has been indicated to be reduced by one-fourth to one-third of the capital cost of the carbon anode potline (Thonstad et al., 2001).

$$2Al_2O_{3(dis)} = 4Al_{(l)} + 3O_{2(g)} \quad (3)$$

The implementation of inert anode to the Hall-Heroult process will also increase its environmental friendliness by eliminating the production of CO, perfluorocarbon gases i.e., CF_4 and C_2F_6, fluoride and dust emissions during anode change, and the elimination of carbon butts (Kvande and Drabloss, 2014). The inert anode technology, however, needs to be underpinned with the significant advancement in materials technology and the heat flow control (Mukhlis et al., 2010).

It is important to be noted that due to the absence of carbon-oxygen reaction that provide energy, the use of inert anode will increase the theoretical energy consumption to 6.54 kWh per kg aluminium production. Lower heat loss, is therefore, required in the cell that used inert anode to be able to have the same amount of energy requirement as the conventional cell.

In the case that heat loss needs to be lowered, the protective frozen ledge will be difficult to be maintained and the sidewall materials will be exposed directly to the very corrosive environments of cryolite bath, the highly reducing molten aluminium zone, as well as the oxidative upper part of the cell due to the existence of air and oxygen at high temperatures. Consequently, the life of the sidewall materials will be significantly reduced. It is obvious that the implementation of inert anode in the cell calls for new ledge-free sidewall materials.

In general, the required properties of the ledge-free sidewalls are very much the same as the required properties of inert anodes except for its electrical conductivity, where in contrast with inert anode, sidewall materials should have low electrical conductivity (Mukhlis, 2015; Yan et. Al., 2011). Spinel based materials, particularly nickel ferrite ($NiFe_2O_4$), have been proposed as inert anode and ledge free sidewall material for aluminium smelter, mainly due to its low solubility and high corrosion resistance against cryolite and high oxidation resistance (Yan et. Al., 2007; Mukhlis et.al., 2010, Longbottom et al., 2014). While these properties make the spinel suit to be applied in both gas zone and cryolite zone, this is not the case for the application in the aluminium zone. It has been predicted thermodynamically that in equilibrium, liquid aluminium will be contaminated by 29.1 mol% Ni and 7.8 mol% Fe when 10 mol of aluminium is in contact with 1 mol $NiFe_2O_4$ at 965 °C. $NiFe_2O_4$ should therefore be combined with other material that have high resistance against molten aluminium if it is to be used as ledge-free sidewall material.

The current paper study the corrosion behaviour of $NiFe_2O_4$, $NiAl_2O_4$ (nickel aluminate), and $MgAl_2O_4$ (magnesium aluminate) in both aluminium and cryolite melts. $NiAl_2O_4$, and $MgAl_2O_4$ were chosen as both are aluminium contained materials, which hypothetically suit to be applied in aluminium zone, low electrical conductivity as well as having similar crystal structure as $NiFe_2O_4$ for the joining compatibility.

MATERIALS AND METHOD

In the present work, the $NiFe_2O_4$, $NiAl_2O_4$, $MgAl_2O_4$ powders were made from its oxide precursors where the details can be found elsewhere (Mukhlis et al, 2011). About 15g of each powder were compacted uniaxially in metal dies at 91 MPa into rectangular bar shape samples, and subsequently sintered under air at 1450 °C for 6 hours for corrosion test. The sintered $NiFe_2O_4$, $NiAl_2O_4$, and $MgAl_2O_4$ sample contained porosity of 12.0%, 42.0%, and 22.4%, respectively, determined by ASTM

C20-00 standard. Higher density $NiAl_2O_4$ (25.5%) porosity and $MgAl_2O_4$ (11.7% porosity) were also tested for comparison.

All surfaces of the sintered bars were grounded up to 800 grits to homogenize the surface roughness and to eliminate the part that may have reacted with the crucible during sintering. Following that, one end of the sintered bar was assembled into a stainless-steel holder that jointed to a stainless-steel rod connected to an overhead electronic stirrer (Figure 1). The assembly were covered with alumina tube to ensure that during experiments, no steel surface is directly exposed to molten bath or molten aluminium and to the atmosphere inside the reactor.

The finger test-type apparatus was used to study the corrosion behaviour of the spinel (Figure 1). A pit furnace was used to melt the electrolyte and aluminium. The molten bath or aluminium melt was hold by a graphite crucible with a dimension of 45 mm inner diameter, 65 mm outer diameter and 175 mm high. Type-K thermocouple that was inserted into the hole drilled in the crucible was used to measure the melt temperature. The gastight closure of the reactor enabled the control of the atmosphere.

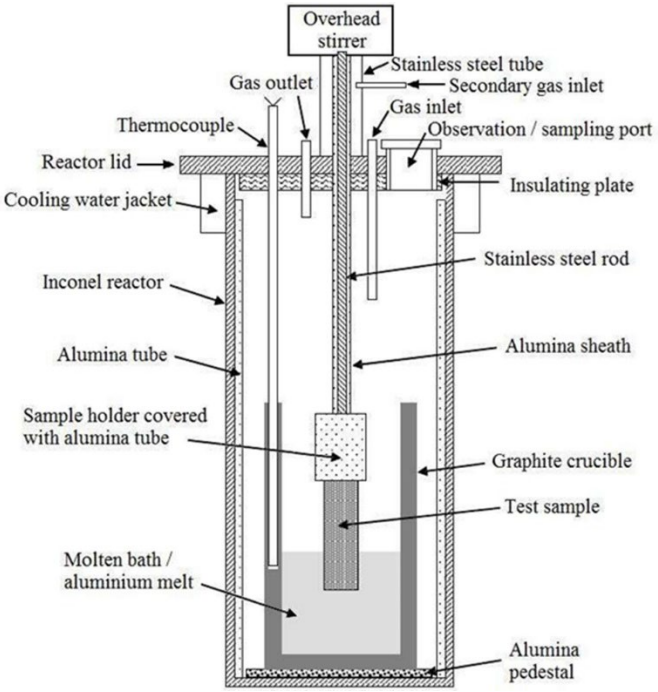

FIG 1 – Schematic diagrams of the stirred finger test apparatus.

To study the corrosion behavior of the spinel materials against Hall-Héroult cell environment, the spinel bar samples were immersed (15mm deep) in a molten aluminium or in cryolite-based melt with a low cryolite ratio of 2.3 (which is equal to 11 wt% excess of AlF_3) contained 6 to 11 wt% alumina addition. The corrosion tests were conducted for 6 hours at a rotation speed of 25 rpm under flowing argon atmosphere of 0.1 l/min. All experiments were carried out at 980 ± 2 °C. During the experiment, samples of cryolite-based bath were taken through the observation port by rapid freezing onto a high purity copper rod which was quickly immersed into the bath, while the aluminium sampling was made using a quartz tube. The sampling was made at 0 minute (just before the immersion), 10 min, 30 min, 1 h, then every hour up to 6 h. The solidified bath/aluminium samples were then used for elemental analysis using Inductively Coupled Plasma (ICP) spectrometry.

RESULTS AND DISCUSSIONS

Corrosion test of $MgAl_2O_4$ in cryolite

Figure 2 shows the photographs of $MgAl_2O_4$ sample with 22.4% porosity that were taken before and after corrosion testing in cryolite-based melt with 2.3 CR contained 11 wt% alumina at 980 °C. No sample left after corrosion testing despite only 15 mm of the sample (out of 34.3mm length of unsealed sample) immersed in the cryolite. It indicates that the reaction between the melt and the sample took place beyond the surface of the sample that had direct contact with the melt.

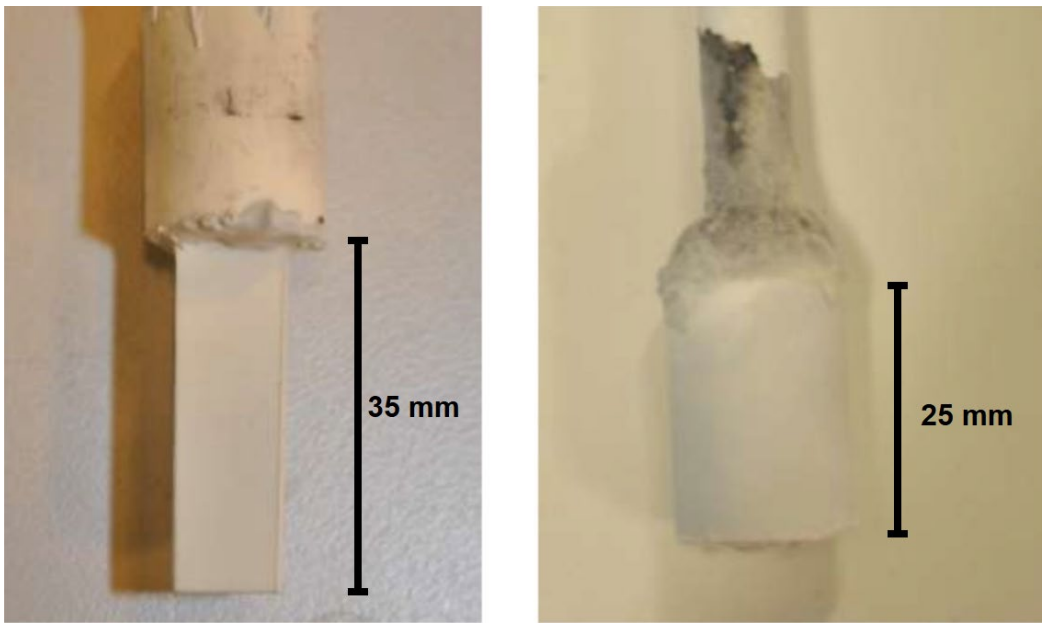

FIG 2 – Sample of $MgAl_2O_4$ with 22.4% porosity: (left) initial sample (b) after corrosion testing.

A liquid in contact with porous substrate may penetrate and progress through the pores of the substrate due to capillarity when the contact angle between the liquid and the substrate is less than 90°. In a separate study conducted by the authors (Mukhlis et al., 2014), it was found that the measured apparent contact angle of electrolyte with 0 wt%, 6wt%, and 11wt% alumina content on $MgAl_2O_4$ substrate was 19.4°, 12.2°, and 9.3°, respectively.

The photographs of the $MgAl_2O_4$ sample with apparent porosity of 11.75 % are shown in Figure 3. Despite there was still some sample left after testing, the denser sample exhibited similar behaviour with the less-dense sample (shown in Figure 2), in which the corrosion proceeded beyond the sample surface that had direct contact with the melt. From 39.7 mm length of the original unsealed sample, only about 10 mm of it remained solid after testing (indicated by S in Figure 3). The rest of the sample were either fully corroded or corroded on its inner part, leaving a hollow structure.

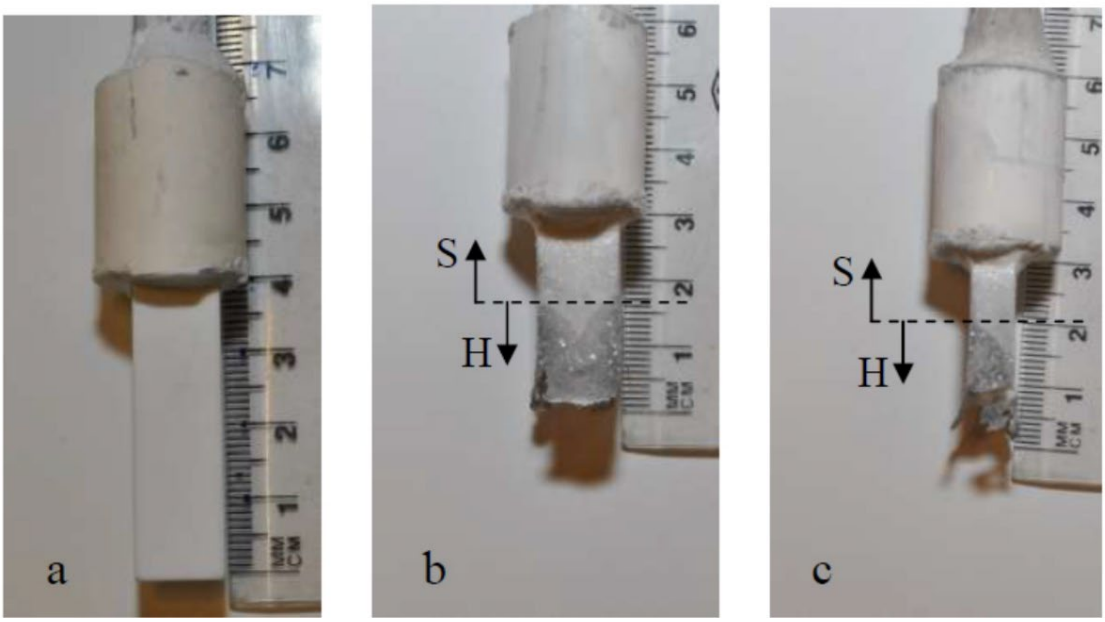

FIG 3 – Photograph of $MgAl_2O_4$ sample with apparent porosity of 11.74 % reacted with cryolite-based melt (CR = 2.3) contained11 wt% alumina at 980 °C: a. before corrosion testing; b. after testing (front view); c. side view. S and H denote solid and hollow, respectively.

The amount of magnesium dissolved in the cryolite-based melt originated from the $MgAl_2O_4$ samples over time as per ICP-AES analysis are plotted in Figure 4.

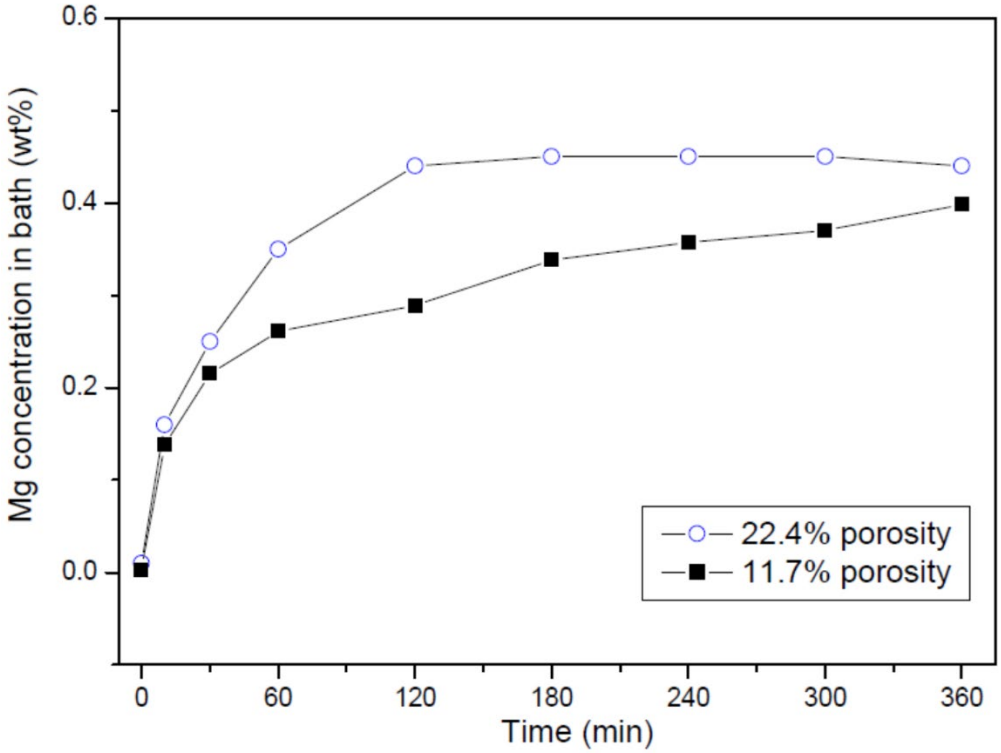

FIG 4 – Elemental analysis of the dissolved magnesium originated from $MgAl_2O_4$ with different porosity level in the cryolite-based melt.

It can be clearly seen from the curves plotted in Figure 4 that the amount of magnesium in the melts rose rapidly at the first 10 minutes in which the gradient of both curves nearly the same. The concentration of magnesium in the melt increased with time at a reduced rate. As the corrosion proceeds, the surface area of the spinel sample that had direct contact with the melt decreased gradually, which may explain the less steep gradient of the curves over the time. In the case of the experiment with the sample with 22.4% porosity, the increase in the magnesium concentration in the melt ceased at a relatively stable value of 0.44 to 0.45 wt% after 120 minutes.

Based on the dimension of the unsealed part of the 22.4% porosity sample, it theoretically contains 0.946 g of magnesium since the magnesium concentration in stoichiometric $MgAl_2O_4$ sample is 17.08 wt%. If the entire unsealed sample is dissolved into 200 g of the cryolite-based melt, the concentration of the magnesium in the melt is expected to be 0.46 wt%, which is very close to the steady state value shown in Figure 4.Through the similar dimensional calculation as above, and by also considering the hollow part of the sample, the expected concentration of magnesium in the melt originated from the 11.75 % porosity sample is 0.36 wt%, which is also close to the maximum concentration of magnesium from the sample shown in Figure 4.

From these calculations, it is concluded that 0.46 wt% is not the solubility limit of the $MgAl_2O_4$ in the cryolite-based electrolyte melt with 2.3 CR contained 11 wt% alumina. It merely indicated that all available samples have been corroded and all magnesium from the sample has been dissolved as supported by Figure 3. It is expected that if there is still available sample of $MgAl_2O_4$ in contact with the melt, the amount of magnesium in the melt will still increase over time until it reached the solubility limit. As for comparison, the solubility limit of MgO in pure cryolite and in cryolite that contain 5 wt% alumina at 1010 °C was found to be 11.65 wt% and 10.6 wt%, respectively (Belyaev et al., 1953; Fuseya and Takeda, 1949).

Corrosion test on the $MgAl_2O_4$ sample with apparent porosity of 22.4% immersed in cryolite-based melt with 2.3 CR contained 6 wt% alumina was conducted to study the effect of alumina concentration in the melt to the corrosion behavior of $MgAl_2O_4$. The concentration of magnesium in the bath over time as per ICP-AES analysis is plotted in Figure 5.

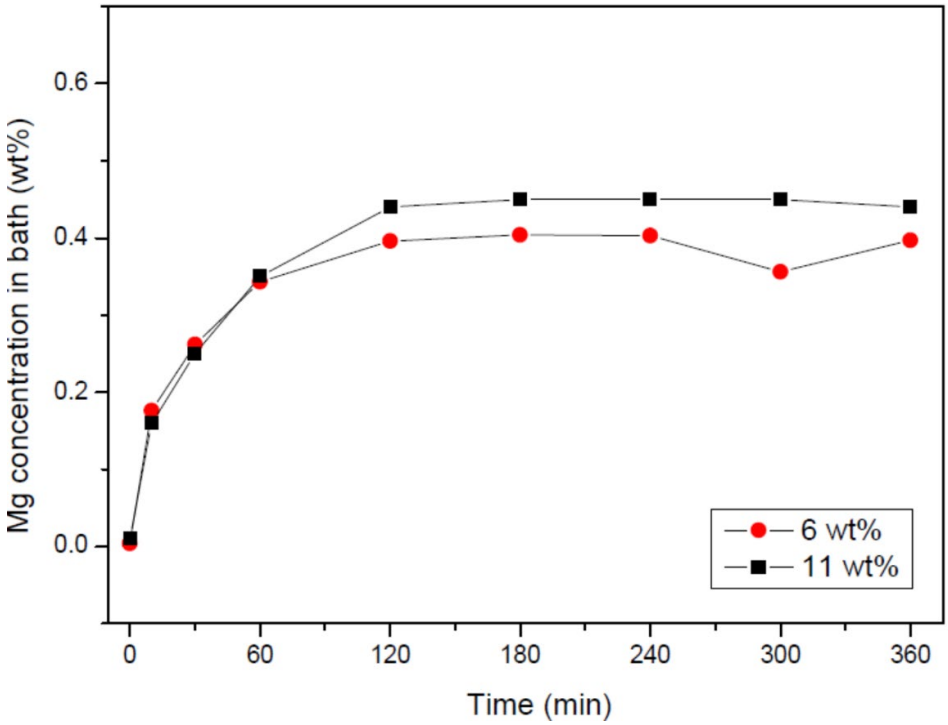

FIG 5 - Elemental analysis of the dissolved magnesium originated from $MgAl_2O_4$ in cryolite-based melts contains different alumina concentration.

As shown in Figure 5, the amount of magnesium in the cryolite-based melt that contain 6 wt% alumina increased sharply for the first 30 minutes and further increased with a reduced rate up to 60 minutes. Up to this period, the gradient of the curve is nearly the same as that for the melt that contain 11 wt% alumina. The magnesium concentration in the melt that contain 6 wt% alumina reached a plateau at 0.4 wt% within 120 minutes. Again, this steady value did not indicate the solubility limit, rather indicate that all available $MgAl_2O_4$ sample has been corroded by the melt and all the magnesium has been dissolved into the melt. It should be noted that the Mg concentration at 300 minute was slightly lower than expected, however, this most likely due to the variation from the measurement e.g., slightly smaller sample hence lower amount of available Mg. While overall trend is quite clear, further test at 300 min immersion is planned to validate the results.

All the above results showing a significant corrosion attack of the melt against magnesium aluminate. These results agree with the thermodynamic study that suggest $MgAl_2O_4$ is not suitable to be applied as ledge free sidewall in contact with the cryolite-based electrolyte.

The typical microstructures of the corroded $MgAl_2O_4$ sample are shown in Figure 6, which is associated with Figure 3.

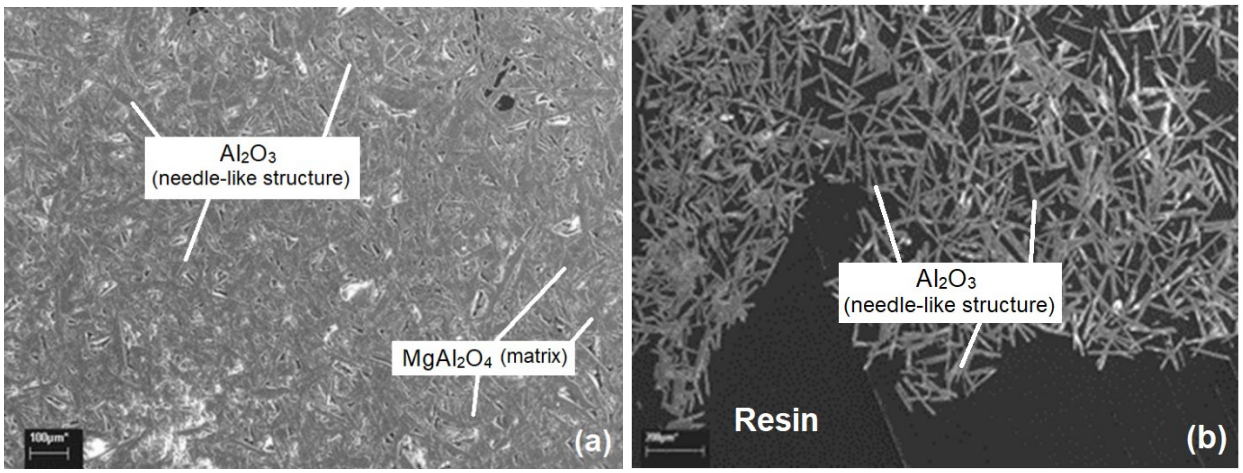

FIG 6 - Microstructure of the $MgAl_2O$ sample that shown in Figure 3: (a) top section of the solid part; (b) bottom section of the hollow part.

As shown in Figure 6, the microstructures of both solid part and hollow part of the sample contained needle like structures that less than 5μm width. The only significant difference is that for solid part (Figure 6a), most of the space in-between the needle like structure was filled with solid structures. The EDS point-analysis suggested that the needle-like structure was Al_2O_3, while the solid structures were solidified electrolyte melts. The presence of the solidified cryolite-based melt - in the top section of the solid part of $MgAl_2O_4$ sample - support the previous hypothesis, which suggested that the melt penetrate into $MgAl_2O_4$ beyond the surface that had direct contact with the melt.

In order to investigate whether there are still un-corroded $MgAl_2O_4$ left in the sample, elemental mapping on the top section of solid part of the sample (refer to Figure 3) has been conducted and the result is shown in Figure 7.

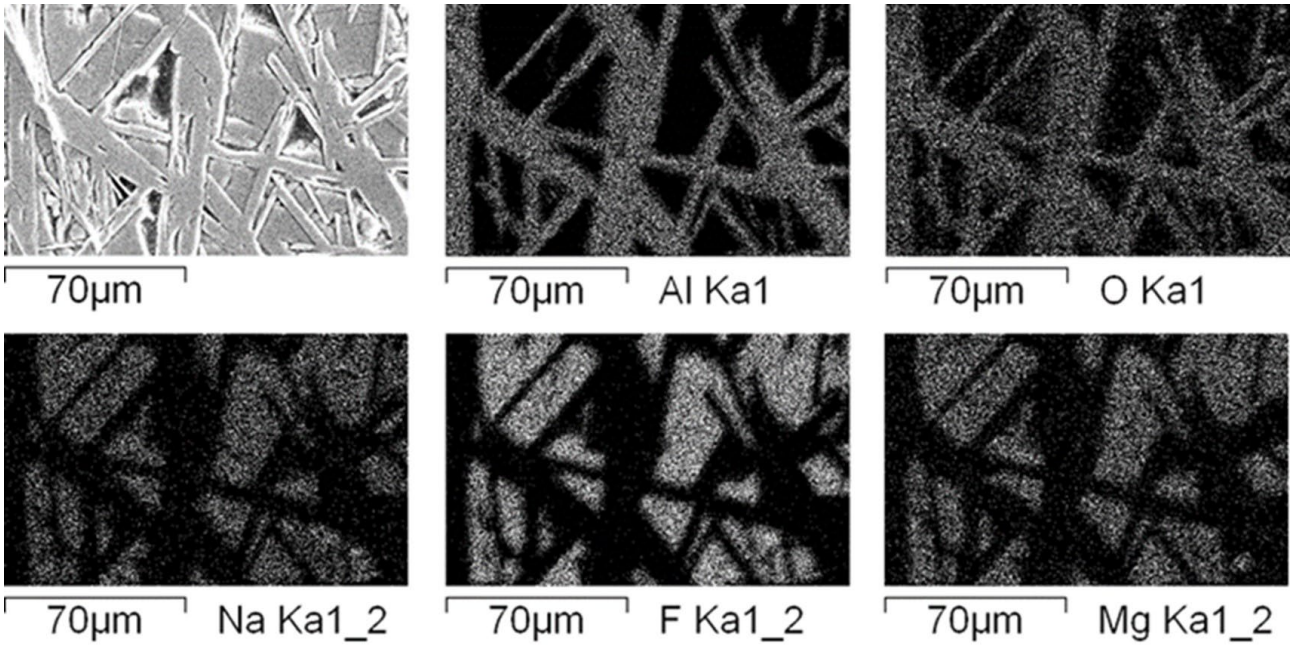

FIG - 7 Elemental mapping on the top section of solid part of $MgAl_2O_4$ sample that shown in Fig.3

Elemental mapping revealed that there were significant compositional changes on the sample after corrosion testing. Most of the aluminium and oxygen were exist in the needle-like structures. On the other hand, most of magnesium was exist in the solid structure surrounded the needle-like structure. Only insignificant trace of magnesium was detected in the needle-like structure. This indicated that no $MgAl_2O_4$ left in the magnesium aluminate sample after 6 hour immersion in the cryolite-based electrolyte. The concentration of magnesium in the stoichiometric $MgAl_2O_4$ is 17.08%. Consequently, for a phase to be qualified to be suggested as $MgAl_2O_4$, the trace of magnesium should be substantial at the place where the trace of both aluminium and oxygen are also significant.

Since most of the magnesium were detected on the area where the sodium and fluorine were substantial, it is argued that the magnesium from $MgAl_2O_4$ was dissolved into the cryolite-based melt. It is also reasonable to conclude that the corrosion mechanism of $MgAl_2O_4$ by cryolite-based melt involve reactions that produce Al_2O_3. One of the plausible reactions is the reaction in Equation 5 below:

$$MgAl_2O_4 + {}^{2}/_{3}\, Na_3AlF_6 = MgF_2 + 2NaF + {}^{4}/_{3}\, Al_2O_3 \qquad (3)$$

This however needs to be studied further.

Corrosion test of $NiAl_2O_4$ in cryolite

Figure 8 shows the pictures of $NiAl_2O_4$ sample before and after corrosion testing in the 2.3 CR cryolite containing 6 wt% Al_2O_3. The $NiAl_2O_4$ samples showed similar behaviour with the $MgAl_2O_4$ samples discussed earlier, in which the part that had direct contact with cryolite – about 15 mm – disintegrated from the sample and went into the melt.

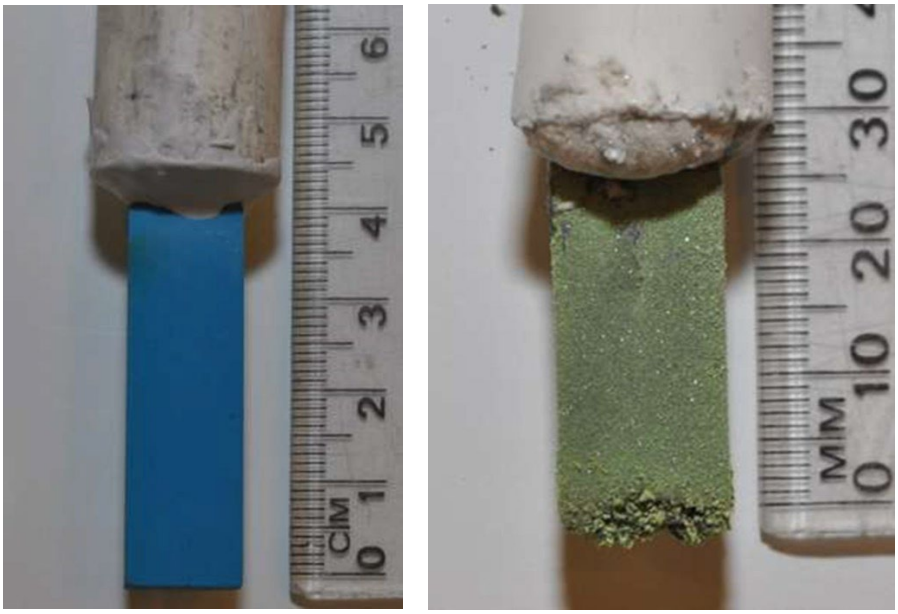

FIG 8 - Typical $NiAl_2O_4$ samples before (left) and after corrosion test (right). The part of the sample that had direct contact with cryolite goes into the melt.

If one considering only the thermodynamics stability of the nickel aluminate in cyolite melts, the effect of the melts to the sample as shown in Figure 8 was rather unexpected. The Gibbs free energy of the reaction between $NiAl_2O_44$ with cryolite at 980 °C is positive (Bale et al., 2022). Moreover, predominance area diagram of the nickel solid phase at 980 °C shown that $NiAl_2O_4$ was predicted to be a stable phase in the alumina-saturated melts. The $NiAl_2O_4$ samples were therefore expected not to be severely corroded, particularly by the alumina-saturated cryolite melts.

The concentration of nickel from $NiAl_2O_4$ in the cryolite melt over the sampling time is plotted in Figure 9. In general, the amount of nickel in the melts increased as the time increase. The total amount of nickel in the melt containing 6 wt% was higher than the nickel in alumina-saturated melt. The rate of the increase in the nickel content was also higher for the melt containing 6 wt% alumina.

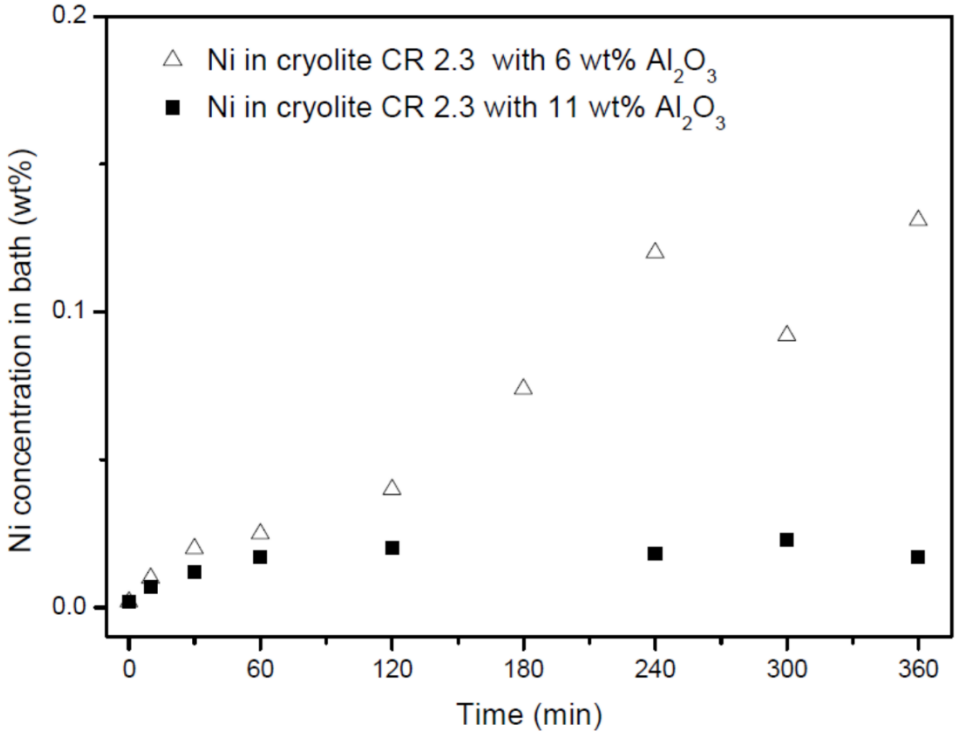

FIG - 9 Concentration of nickel originated from $NiAl_2O_4$ in cryolite-based melts contains different alumina concentration.

According to the previous research conducted by Lorentsen (2000), the saturation concentration, i.e., solubility limit, of nickel from $NiAl_2O_4$ in cryolite containing 6 wt% and 11 wt% alumina is 3.8 x 10^{-2} and 0.86 x 10^{-2} wt%, respectively. Surprisingly, after 6 hours of experiment, the nickel contents in the melts were much beyond the solubility limit. The concentration of nickel in the melt containing 6 wt% and 11 wt% alumina was found to be 0.13 and 0.02 wt%. Owing to this, it was argued that the corrosion of $NiAl_2O_4$ by cryolite-based melts in current study was not only due to the dissolution of spinel constituents into the melts, but also due to the erosion on the spinel by the melts. The concentrations of nickel in the melt found in current study were suggested as the summation of the dissolved nickel in the melt and the nickel aluminate particles inside the melts due to erosion. By considering the integrity and the density of $NiAl_2O_4$ that were very low, it was reasonable to expect the high erosion level on the sample.

The microstructure of the $NiAl_2O_4$ sample after corrosion testing is shown in Figure 10. The microstructure shown in Figure 10a is associated with the top section of the solid part of the sample closer to sample holder, while Figure 10b is associated with the bottom section of the sample near to the immersed section (refer to Figure 8).

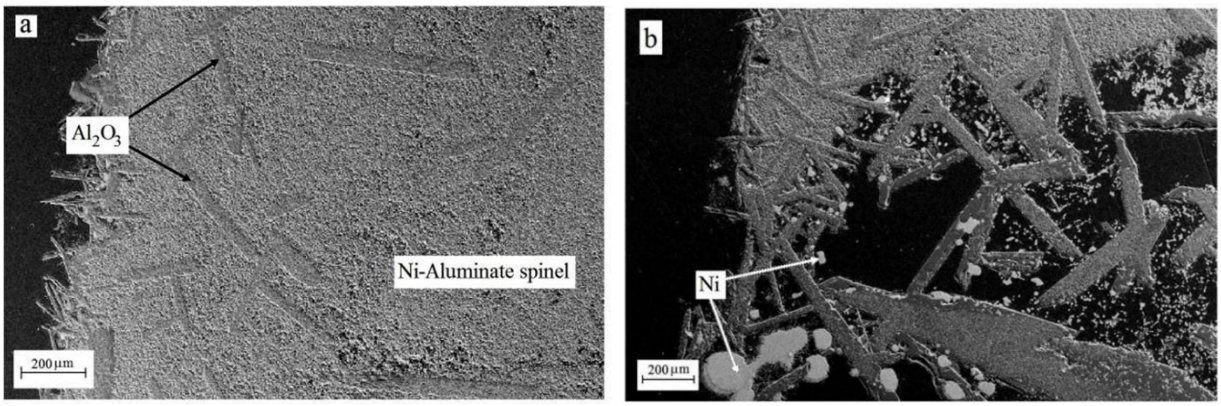

FIG 10 - Microstructure of $NiAl_2O_4$ sample after corrosion testing: (a) section of the sample closer to sample holder; (b) section of the sample near to the immersed section.

Both sections of the corrosion-tested $NiAl_2O_4$ sample in Figure 10a and 10b contained needle like-structures which are surrounded by the solid structures. Interestingly, in addition to these microstructures, there was some roundish white microstructure found in the section of the sample near to the immersed section (Figure 10b). EDS point-analysis suggested that the needle like structure was Al_2O_3. The solid structure was suggested as nickel aluminate as it contains Ni, Al and O; while the roundish white microstructure was suggested as metal since nickel was the only element detected in the spot. To further study the microstructure, EDS elemental mapping had been conducted on the zoomed part of the middle section and the bottom section as shown in Figure 11 and Figure 12, respectively.

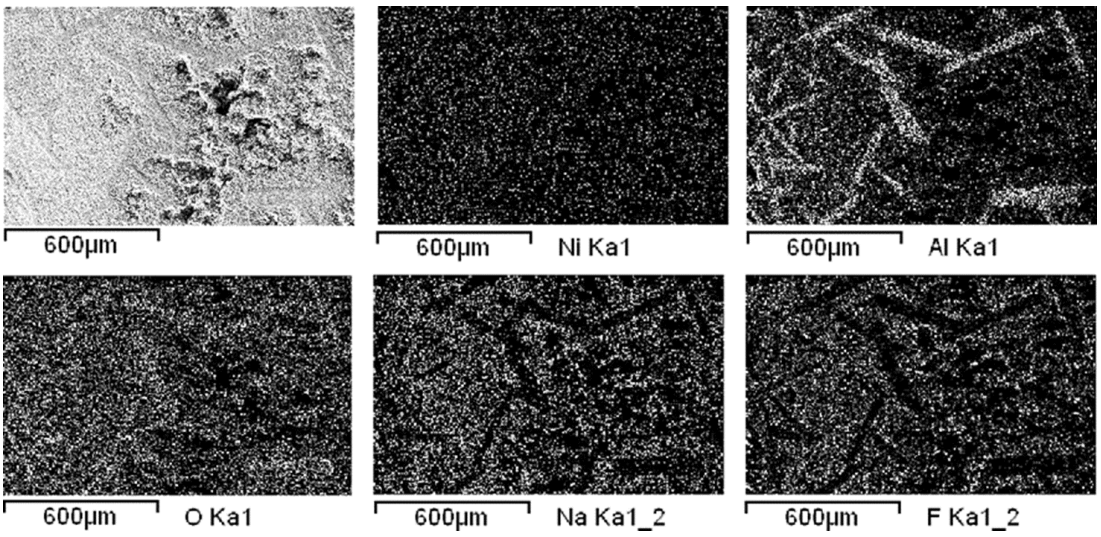

FIG 11 - EDS elemental mapping on the middle section of the corrosion-tested $NiAl_2O_4$ sample.

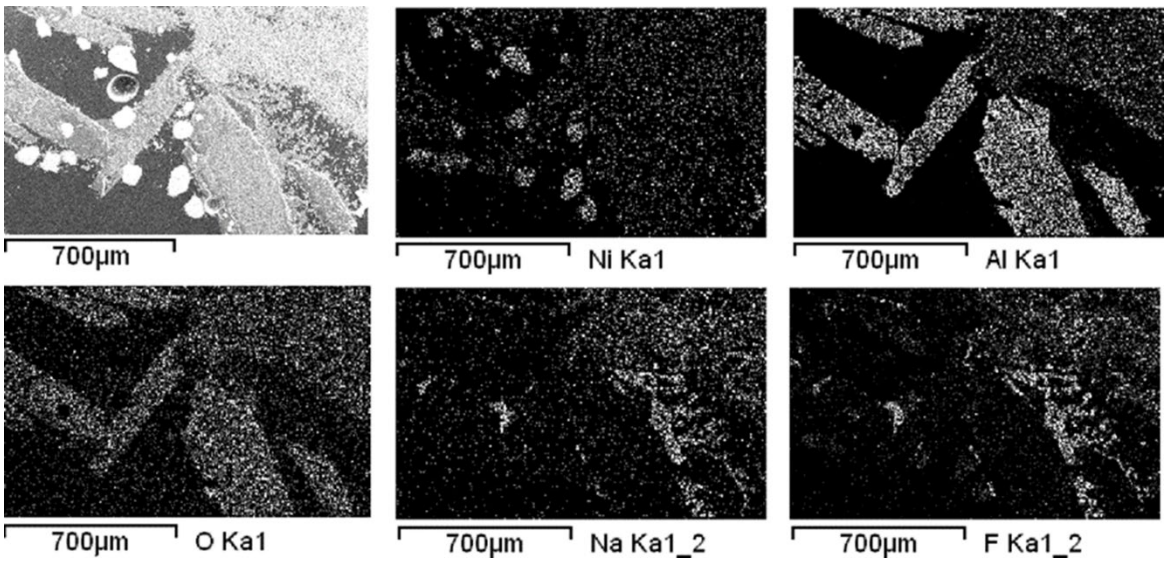

FIG 12 - EDS elemental mapping on the section of the corrosion-tested $NiAl_2O_4$ sample close to the immersed section.

The EDS elemental mapping results confirmed that there were sodium and fluorine elements exist in the solid structure that surrounded the Al_2O_3. This suggests that the cryolite penetrated into the $NiAl_2O_4$ sample beyond the section where the sample had direct contact with the molten bath. However, unlike the $MgAl_2O_4$ where there was no magnesium aluminate left in the sample after corrosion tested, there were still nickel aluminate left in the $NiAl_2O_4$ sample. This support the hypothesis that suggests the corrosion of the $NiAl_2O_4$ sample was not only due to dissolution of the spinel constituent by the melt, but also due to erosion.

Since there were significant amount of Al_2O_3 found in the corrosion-tested $NiAl_2O_4$ sample, the reaction in Equation 6 below seems plausible.

$$NiAl_2O_4 + {}^{2}/_{3}\, Na_3AlF_6 = NiF_2 + 2NaF + {}^{4}/_{3}\, Al_2O_3 \qquad (6)$$

The presence of metallic nickel in the bottom section of the sample suggested that NiF_2 dissociated into Ni. The explanation on how the nickel was formed need further study.

Corrosion test of $MgAl_2O_4$ in cryolite

The pictures of $NiFe_2O_4$ sample before and after corrosion testing are shown in Figure 13. The typical sample before test is shown in Figure 13a, while the appearance of the sample after 6 hours immersion in the cryolite-based melts with CR 2.3 containing 6 wt% alumina and 11 wt% alumina is shown in Figure 13b and Figure 13c, respectively.

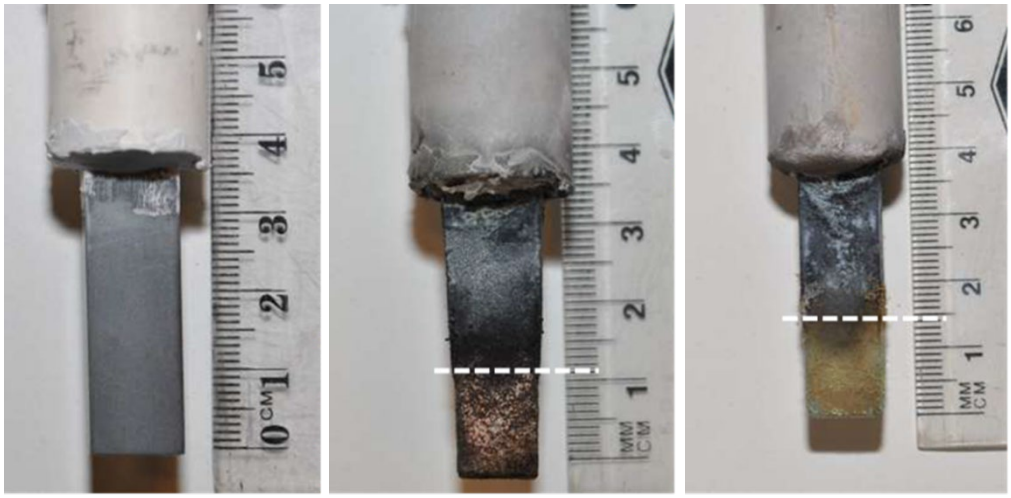

FIG 13 - $NiFe_2O_4$ sample for corrosion test in cryolite-based melts: (a) Typical sample before test; (b) after immersion in melt containing 6 wt% alumina; (c) after immersion in melt containing 11 wt% alumina. The white lines in (b) and (c) indicate the depth of immersion.

On the contrary to the cases of $MgAl_2O_4$ and $NiAl_2O_4$ samples, most of the immersed sections of the $NiFe_2O_4$ samples were still retained. There were indeed noticeable discolorations on the immersed sections. However, the dimension of the section immersed in the melts containing 6 wt% alumina i.e. length, width and thickness was slightly reduced, while the dimension of the section immersed in the melts containing 11 wt% alumina showed no change. This indicated that in cryolite- based melts, particularly in the alumina-saturated melt, $NiFe_2O_4$ exhibited the lowest corrosion compared to $MgAl_2O_4$ and $NiAl_2O_4$.

The change in the concentration of nickel ferrite constituents in the melt over time is plotted in Figure 14. In general, the concentration of the constituent increased as the time increase.

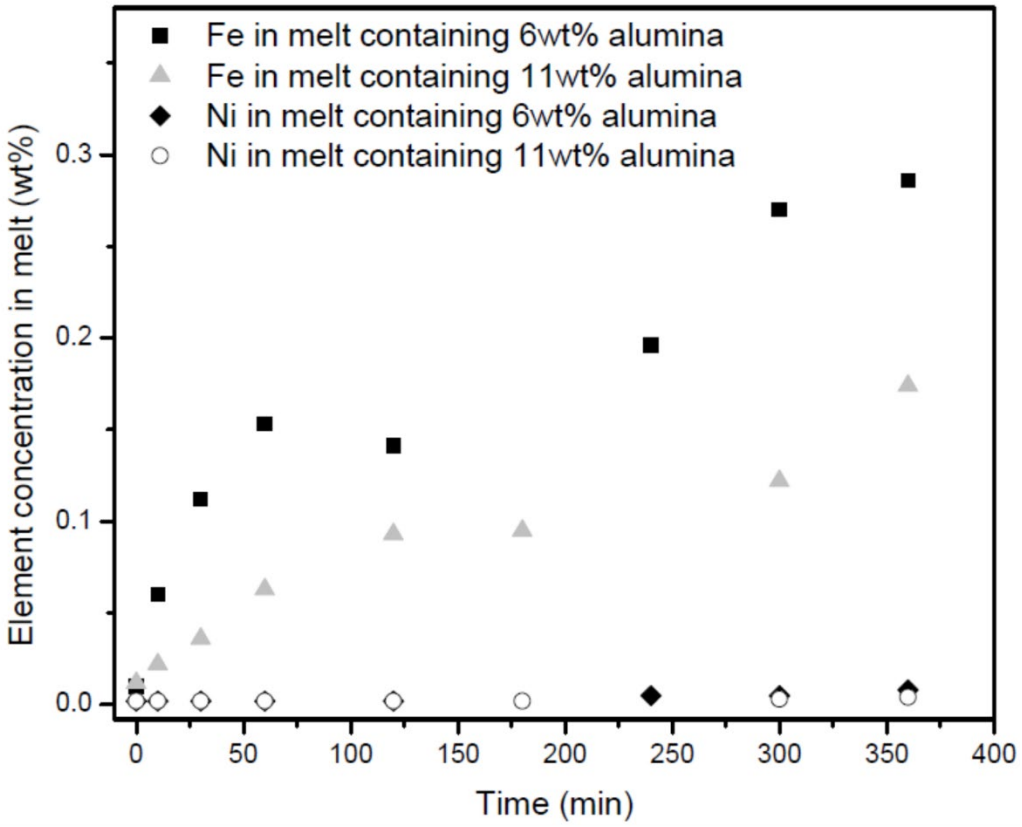

FIG 14 - Concentration of nickel ferrite constituents in cryolite-based melts as a function of time at 980 °C.

It can be seen clearly in Figure 14 that the change in the iron concentration was considerably more rapid than the change in the nickel concentration. In both melts containing 6 wt% and 11 wt% alumina, the final iron concentration after 6 hours test was also significantly higher than nickel and it did not reflect the stoichiometric ratio of iron to nickel in nickel ferrite. These results indicate preferential dissolution of iron in the melts, which agreed with other' studies (Yan et al., 2007; Olsen and Thonstad, 1999a and 1999b). Compared to the melt containing 6 wt% alumina, the total concentration of $NiFe_2O_4$ constituents in the alumina-saturated melt was lower. The rate at which the concentration of the constituent changed over the time was also lower in the alumina-saturated melt. This indicates that the corrosion resistant of nickel ferrite increased as the alumina concentration in the melt increase.

The typical microstructure of nickel ferrite sample after 6 hours corrosion test and its associated EDS elemental mapping are shown in Figure 15a and Figure 15b, respectively.

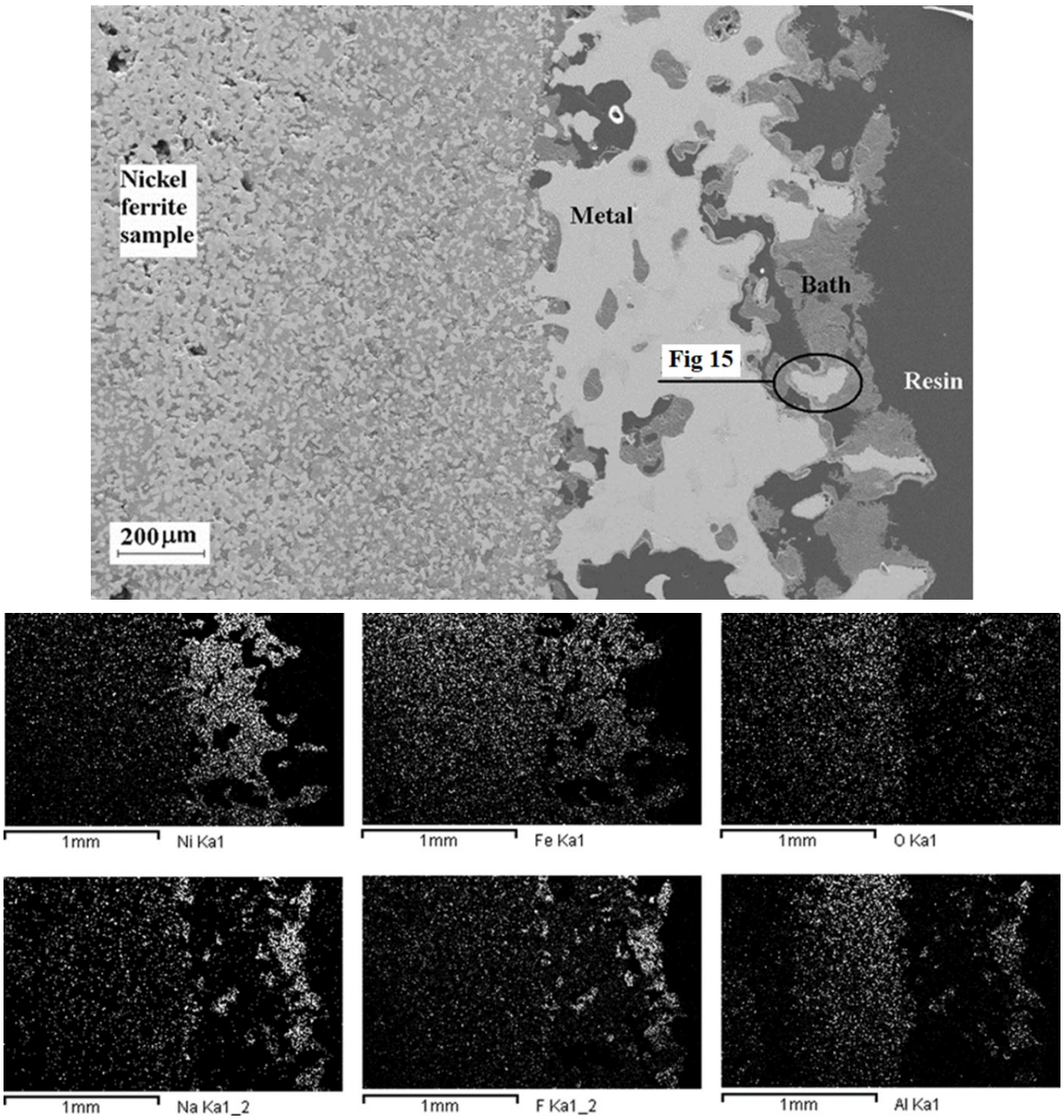

FIG - 15 (a) Typical microstructure of nickel ferrite sample near the sample-bath interface after 6 hours corrosion testing in non-saturated cyolite based-melt; (b) EDS elemental mapping confirming the presence of Fe-Ni metallic phase at the sample-bath interface.

Figure 15 shows that there were significant composition changes occurring near the sample-bath interface where Ni-Fe metallic phase was formed. The presence of sodium, fluoride and aluminium in the bulk nickel ferrite sample indicated that the bath penetrated into the sample. A higher magnification of the area designated as Fig 16 in Figure 15 revealed that there were several different microstructures surrounding the Ni-Fe metallic phases as shown in Figure 16.

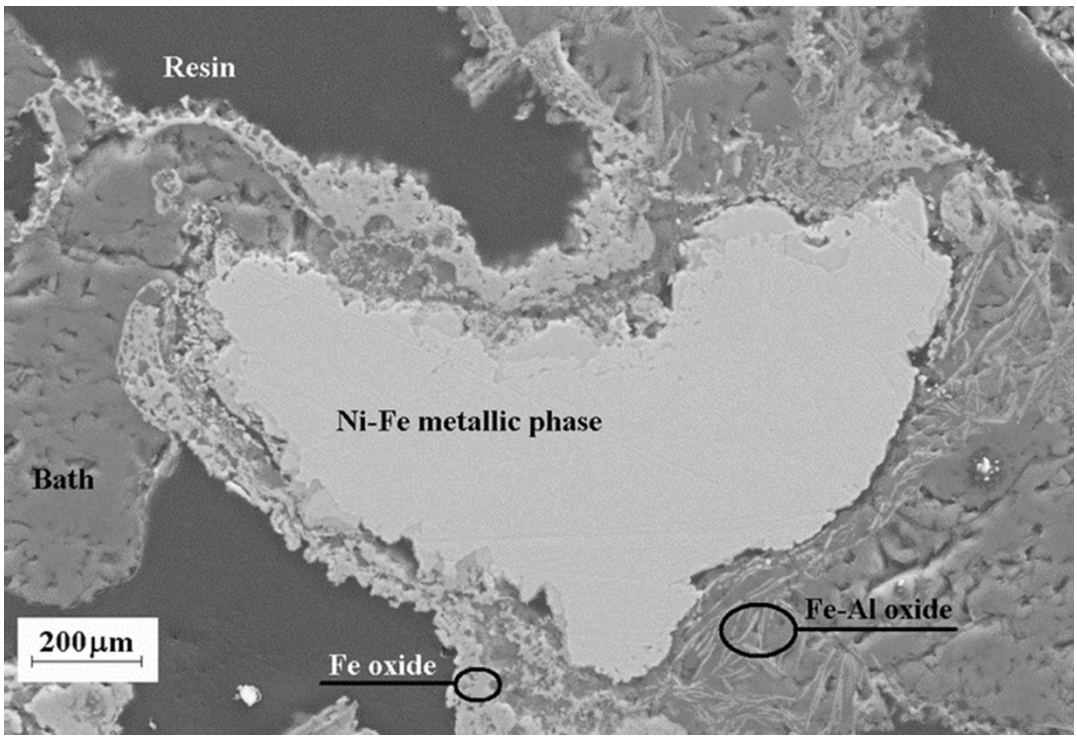

FIG - 16 Higher magnification of the area designated as Fig 16 in Figure 15. The phases were suggested by EDS point analysis and elemental mapping.

Dissolution of spinel constituents into cryolite-based melt

The kinetics and the dissolution rate of ferrite and aluminate spinels into cryolite-based melts have been studied elsewhere by the author (Mukhlis, 2015). Plot of $(V/A)(\ln[(c_{sat}-c_0)/(c_{sat}-c)])$ against time time (t) were used to determine the mass transfer coefficient rate (k value) of the process. Here, V is the volume of electrolyte in m^3, A is the surface area of spinel sample that have direct contact with melt in m^2, c_{sat} is the initial amount of spinel constituent in the melt plus the maximum amount of the spinel constituent that can enter the melt from the sample in wt%, $c(t)$ is the time dependent concentration of species in the electrolyte in wt%, c_0 is the initial concentration of spinel constituent in melt, and k is the mass transfer coefficient of species from spinel to electrolyte in m/s.

The same approach, i.e. plot of $(V/A)(\ln[(c_{sat}-c_0)/(c_{sat}-c)])$ against time (t), using the data shown in Figure 14, was applied in the current study to determine the k value which then used to calculate the corrosion rate. The projected annual corrosion rate for each spinel samples is tabulated in Table 1.

Table 1 Projected corrosion rate of spinels against cryolite-based melt with CR 2.3 at 980 °C.

Sample	Constituent	Alumina concentration in melt	Projected corrosion rate (cm/year)
$MgAl_2O_4$	Mg	6 wt%	644×10^3
		11 wt%	798×10^3
$NiAl_2O_4$	Ni	6 wt%	4.7×10^3
		11 wt%	1.03×10^3
$NiFe_2O_4$	Ni + Fe	6 wt%	947×10^3
		11 wt%	461×10^3

Projected corrosion rate was calculated based on the assumption that 1 year is equal to 365 days. The value for $NiFe_2O_4$ is the combination of values for Ni + Fe. As seen in Table 1, the projected corrosion rates for all spinel in cryolite-based electrolyte were very high.

Corrosion of $NiFe_2O_4$, $NiAl_2O_4$, $MgAl_2O_4$ in molten aluminium

The results of the finger test experiments of spinels in molten aluminium at 980 °C through ICP analysis are shown in Figure 17. The concentration of spinel constituents - i.e. magnesium, nickel, and iron - in aluminium were plotted against the sampling time. The non-zero concentration of the constituents at t = 0 represented the impurity levels of the aluminium used in current study before the immersion of the spinel sample, which agreed with the specification from the manufacturer.

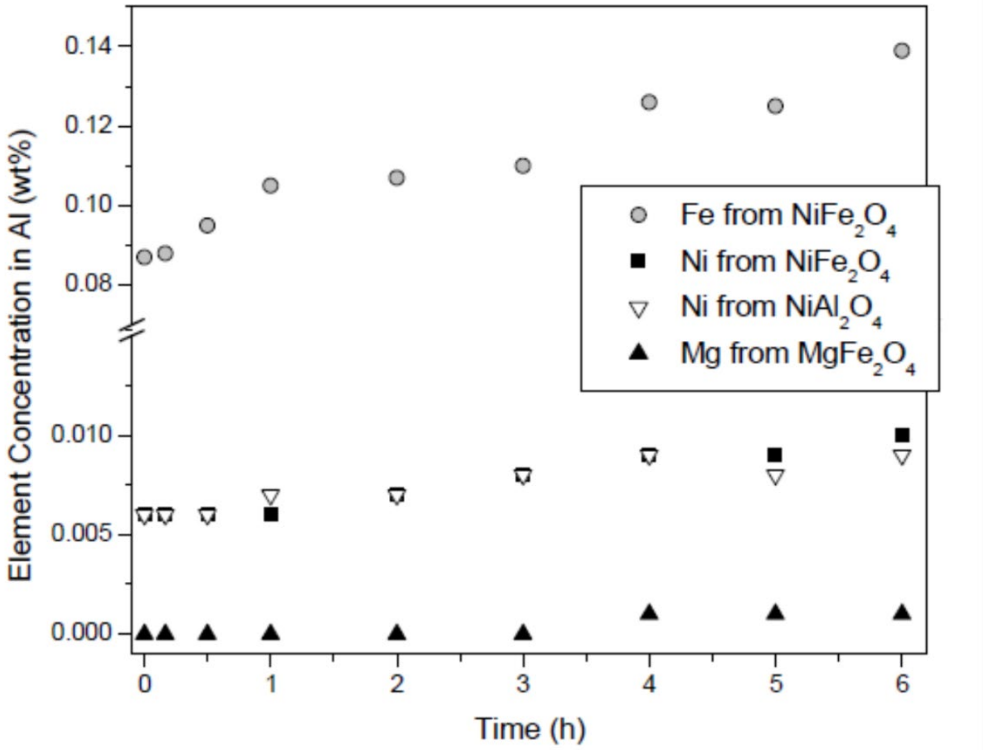

FIG 17 - Element concentrations in molten aluminium from spinel sample.

One can see from Figure 17 that in general, the concentrations of the spinel constituents in aluminium increased with increasing time up to 6 hours. In agreement with the thermodynamics analysis, $MgAl_2O_4$ sample showed the lowest level of contamination to the aluminium at the end of the 6 hours experiments. The amount of nickel contaminations from $NiAl_2O_4$ and $NiFe_2O_4$ were at the same order of magnitude. The highest contamination in aluminium determined by current study was iron that came from nickel ferrite sample, which reached 0.14 wt% after 6 hours immersion; that was two orders of magnitude higher than the magnesium contamination originated from magnesium aluminate.

Similar to the evaluation on the Spinel-Cryolite system, the rate constant of the corrosion of the spinel due to dissolution of its constituents into molten aluminium (i.e. mass transfer coefficient) was evaluated from the experimental data points plotted in the coordinates of $(V/A)(\ln[(c_{sat}-c_0)/(c_{sat}-c)])$ against time (t).

In contrast with the spinel-cryolite system, there were no visible changes of dimension on the spinel sample after 6 hours corrosion test in molten aluminium. Therefore, the confidence level of the corrosion rate value of the spinel-aluminium system is higher than that of spinel- cryolite system. The c_{sat} for Mg, Ni and Fe used in current study were 100, 38.2, and15.5 wt%, respectively, which was determined from the associated Mg-Al, Ni-Al, and Fe-Al phase diagrams constructed using Factsage 6.4.

Through the identical approach as the calculation for spinel-cryolite melt system, the projected values of the maximum corrosion rate of spinel due to dissolution of its constituent into molten aluminium were calculated to be 0.3, 2.6, and 78.4 cm/year for $MgAl_2O_4$, $NiAl_2O_4$, and $NiFe_2O_4$, respectively. It should be noted that the corrosion rate for $NiFe_2O_4$ is the summation of the dissolution rate of nickel and iron (refer to Table 2).

Table 2 Mass transfer coefficient and projected maximum corrosion rate of spinels constituents against molten aluminium.

Sample	Constituent	Element concentration in Al after 6h test	Highest possible mass transfer coefficient	Projected maximum corrosion rate
$MgAl_2O_4$	Mg	0.1 x 10^{-2} wt%	10.0 x 10^{-11} m/s	0.3 cm/year
$NiAl_2O_4$	Ni	0.9 x 10^{-2} wt%	8.25 x 10^{-10} m/s	2.6 cm/year
$NiFe_2O_4$	Ni	1.0 x 10^{-2} wt%	7.26 x 10^{-10} m/s	2.3 cm/year
	Fe	13.9 x 10^{-2} wt%	2.41 x 10^{-8} m/s	76.1 cm/year

Based on the data tabulated in Table 3, one can conclude that in the molten aluminium environment, $MgAl_2O_4$ showed the best performance as it had the lowest corrosion rate as well as the lowest contamination to the molten aluminium. The data also revealed that $NiFe_2O_4$ will not be suitable to be applied in direct contact with molten aluminium as it will promote substantial contamination to the metal. The projected corrosion rate of $NiFe_2O_4$ was also significantly high, about 50 times higher than the acceptable corrosion rate of the materials applied in the Hall-Héroult cell, which is supposed to be not higher than 1 to 1.5 cm/year (Xiao et al., 1996; Oye and Welch, 1998; and Galasiu et al., 2007).The kinetics and the dissolution rate of ferrite and aluminate spinels into cryolite-based melts have

CONCLUSIONS

The observation on the spinel samples after corrosion testing indicate that $NiFe_2O_4$ has the best corrosion resistance against acidic cryolite-based melt (CR 2.3) compared to the other spinels. After 6 hours immersion in the melt at 980°C, there were insignificant changes in the dimension of $NiFe_2O_4$ sample from its initial dimension. In contrast, the $MgAl_2O_4$ and $NiAl_2O_4$ samples were corroded heavily. All part of the samples that immersed in the melt disintegrated from the sample bulk and entered the melt. In the case of corrosion test against aluminium, all spinel samples (i.e. magnesium aluminate, nickel aluminate, and nickel ferrite) showed no dimensional changes macroscopically.

The projected corrosion rates, assuming linear behaviour, of the spinels against the bath were higher than the acceptable corrosion rate of materials applied in the aluminium smelter application. The projected corrosion rates of the spinels against molten aluminium, on the other hand was acceptable except for $NiFe_2O_4$. It was found that the corrosion rate for magnesium aluminate, nickel aluminate, and nickel ferrite against molten aluminium were 0.3, 2.6, and 78.4 cm/year. This result is in agreement with the thermodynamic analysis that suggests $MgAl_2O_4$ is the most stable spinel in aluminium environment compared to the other two spinels.

The nickel in the cryolite-based melt that originated from $NiAl_2O_4$ sample were found to be higher than the solubility limit of the respective element in the given bath composition. This indicate that the corrosion of the spinel not only due to dissolution of the spinel constituent into the bath, but also enhanced with the erosion of the sample. This was supported with the observation on the $NiAl_2O_4$ sample after corrosion test, where all part of the sample immersed in the bath (about 15 mm) was disintegrated from the sample bulk.

The presence of sodium and fluorine in the top part of the samples that far from the immersed section indicate that the cryolite-based melt had a good wettability against spinels; particularly $MgAl_2O_4$ and $NiAl_2O_4$. When the melt wetted the sample, it can readily penetrate into the sample through the sample pores.

The increase of the spinel constituent in the bath over the time for the denser spinel sample was found to be slower than that of high porosity sample. It is then recommended to use a much denser spinel for the aluminium smelter application. The use of denser spinel will reduce the erosion-induced corrosion and the penetration of the bath into the spinel. This however will hinder its industrial application since it will increase the cost and add more complexities to the industry.

Microstructural study on the corroded spinel sample suggested that $MgAl_2O_4$ spinel was unstable in the cryolite-based melt environment as there were no spinel left in the sample even at the section that far from the immersed part of the sample. All magnesium dissolved into the bath, leaving only aluminium oxide in the sample. $NiAl_2O_4$ and $NiFe_2O_4$ appeared to have better resistance to the reaction against cryolite-based melt (kinetically), particularly against alumina-saturated melt, as there were still plenty of spinel left in the sample after 6 hours immersion. The $NiAl_2O_4$ samples however were susceptible to erosion.

ACKNOWLEDGEMENTS

The first author acknowledges Swinburne University of Technology and Commonwealth Scientific and Industrial Research Organisation (CSIRO) for providing scholarship to conduct the study. The co-supervision of Prof. Geoffrey Brooks, Dr. Kathie McGregor, and Dr. Xiao Yong Yan in the study are also acknowledged.

REFERENCES

Bale, C. W., Chartrand, P., Degterov, S. A., Eriksson, G., Hack, K., Ben Mahfoud, R., Melancon, J., Pelton, A. D. & Petersen, S. (2002). FactSage thermochemical software and databases. *Calphad*, *26*(2), 189-228.

Belyaev, A. I., Rapoport, M. B., & Firsanova, L. A. 1953. *Elektrometallurgiya alyuminiya*. Moscow: Metallurgizdat. (From Grjotheim et al., 1982).

Fuseya, G. & Takeda, B. 1949. *Journal of Electrochemical Society Japan, 17*, 31. (From Grjotheim et al., 1982).

Galasiu, I., Galasiu, R., & Thonstad, J. 2007. *Inert anodes for aluminium electrolysis*. Dusseldorf: Aluminium-Verlag.

Grojtheim, K., Krohn, C., Malinovsky, M., Matiasovsky, K., & Thonstad, J. 1982. *Aluminium Electrolysis - Fundamentals of the Hall-Héroult Process*. Dusseldorf: Aluminium-Verlag.

Haraldsson, J. and Johansson, M.T., 2020. Effects on primary energy use, greenhouse gas emissions and related costs from improving energy end-use efficiency in the electrolysis in primary aluminium production. *Energy Efficiency*, *13*(7), pp.1299-1314.

Kvande, H., & Drablos, P. A., 2014. The Aluminum Smelting Process and Innovative Alternative Technologies. *Journal of Occupational and Environmental Medicine, 56,* S23-S32.

Longbottom, R. J., Nightingale, S. A., & Monaghan, B. J. 2014. Thermodynamic considerations of the corrosion of nickel ferrite refractory by Na3AlF6-AlF3-CaF2-Al2O3 bath. Mineral Processing and Extractive Metallurgy (Trans. Inst. Min Metall. C), 123(2), 93-103.

Lorentsen, O. A. 2000. *Behaviour of nickel, iron and copper by application of inert anodes in aluminium production*. dr. ing. Thesis. Trondheim: Department of Electrochemistry, Norwegian University of Science and Technology.

Mukhlis, R., Rhamdhani, M., & Brooks, G., 2010. Sidewall materials for the Hall-Heroult process. *Light Metals 2010,* 883-888.

Mukhlis, R. Z., Rhamdhani, M. A., Brooks, G. A., & Yan, X. Y., 2011. Fabrication of spinel composites for sidewall of Al smelter application. In *European Metallurgical Conference 2011*, 865-880.

Mukhlis, R.Z., Rhamdhani, M.A., Brooks, G. and McGregor, K., 2014. Wetting characteristics of cryolite-based melts on spinels substrate. *Light Metals 2014*, pp.609-614.

Mukhlis, R. Z., 2015. Analysis of Spinel Materials for Aluminium Smelter Applications. Doctoral dissertation, Swinburne University of Technology Melbourne, Australia.

Olsen, E., & Thonstad, J. 1999a. Nickel ferrite as inert anodes in aluminium electrolysis: Part I Material fabrication and preliminary testing. *Journal of Applied Electrochemistry*, *29*(3), 293-299.

Olsen, E., & Thonstad, J. (1999b). Nickel ferrite as inert anodes in aluminium electrolysis: Part II material performance and long-term testing. *Journal of applied electrochemistry*, *29*(3), 301-311.

Schwarz, H. G. (2008). Technology diffusion in metal industries: driving forces and barriers in the German aluminium smelting sector. *Journal of Cleaner Production, 16(1),* S37-S49.

Thonstad, J., Fellner, P., Haarberg, G. M., Hives, J., Kvande, H., & Sterten, A (2001). Aluminum electrolysis. *Fundamentals of the Hall-Heroult Process.* Dusseldorf: Aluminum-Verlag.

Welch, B. J., & May, A. E. 1987. Materials problems in Hall-Héroult cells. In *8th International Light Metals Congress*, 120-125.

Yan, X. Y., Pownceby, M. I., & Brooks, G. 2007. Corrosion behavior of nickel ferrite-based ceramics for aluminum electrolysis cells. *Light Metals 2007*, 909-913.

Yan, X. Y., Mukhlis, R. Z., Rhamdhani, M. A., & Brooks, G. A., 2011. Aluminate spinels as sidewall linings for aluminum smelters. *Light Metals 2011*, 1085-1090.